I&EC research
Industrial & Engineering Chemistry Research

Article

pubs.acs.org/IECR

Graphitic Biocarbon from Metal-Catalyzed Hydrothermal Carbonization of Lignin

Muslum Demir,[†,#] Zafer Kahveci,[∥] Burak Aksoy,[‡] Naveen K. R. Palapati,[§] Arunkumar Subramanian,[§] Harry T. Cullinan,[‡] Hani M. El-Kaderi,[∥] Charles T. Harris,[⊥] and Ram B. Gupta*[,†]

[†]Department of Chemical and Life Science Engineering, [§]Department of Mechanical and Nuclear Engineering, and [∥]Department of Chemistry, Virginia Commonwealth University, Richmond, Virginia 23284, United States

[‡]Alabama Center for Paper and Bioresource Engineering, Dept. of Chemical Engineering, Auburn University, Auburn, Alabama 36849, United States

[⊥]Center for Integrated Nanotechnologies, Sandia National Laboratories, Albuquerque, New Mexico 87185, United States

ABSTRACT: Lignin is a high-volume byproduct from the pulp and paper industry and is currently burned to generate electricity and process heat. The industry has been searching for high value-added uses of lignin to improve the process economics. In addition, battery manufacturers are seeking nonfossil sources of graphitic carbon for environmental sustainability. In this work, lignin (which is a cross-linked polymer of phenols, a component of biomass) is converted into graphitic porous carbon using a two-step conversion. Lignin is first carbonized in water at 300 °C and 1500 psi to produce biochar, which is then graphitized using a metal nitrate catalyst at 900−1100 °C in an inert gas at 15 psi. Graphitization effectiveness of three different catalysts—iron, cobalt, and manganese nitrates—is examined. The product is analyzed for morphology, thermal stability, surface properties, and electrical conductivity. Both temperature and catalyst type influenced the degree of graphitization. A good quality graphitic carbon was obtained using catalysis by $Mn(NO_3)_2$ at 900 °C and $Co(NO_3)_2$ at 1100 °C.

1. INTRODUCTION

Lignin, a commonly occurring natural material,[1,2] is a complex polymer of aromatic alcohols.[3] It is mainly composed of coniferyl alcohol, sinapyl-based alcohols, and their derivatives, with small amounts of coumaryl alcohol derivatives.[4] The monomeric units of lignin are linked to each other mostly by ether linkages and carbon-to-carbon bonds (Figure 1).[5] Typically, woody plants contain as much as 20−30 wt % lignin.[6] Hence, lignin is generated in large quantities (>50 million tons/year) in pulping spent liquor. This lignin is typically concentrated and burnt in pulp mills for steam generation. At present, only about 2% of the lignin produced in the pulp and paper industry is commercially used; about 1 million tons/year of commercial lignosulfonates originate from sulfite pulping and <0.1 million tons/year from kraft pulping.[7,8] Current applications of lignin are in concrete admixtures, animal feed pellets, and roadside dust control, as dispersing, wetting, binding agents, etc.[9−14] As the supply of the unused lignin is much greater, there has been a renewed interest in the development of new value-added products from lignin.[15]

Graphite is conventionally obtained by high-heat treatment (~3000 °C) or stress graphitization of carbon-rich feedstocks.[16] Due to the severity of process conditions, this method is expensive, complex, and limited in scalability. In addition, the produced graphite has a poor porosity due to nonexistent surface activation during the graphitization step. The graphitization temperature can be significantly reduced (down to ~1000 °C) by use of transition-metal catalysts such as Fe, Ti, Co, Ni, and Mn.[17−21] Metal impregnation during the graphitization process can also increase the porosity.[22−26] In recent years, several research groups have utilized biomass feedstock to produce graphitic porous carbons that have a

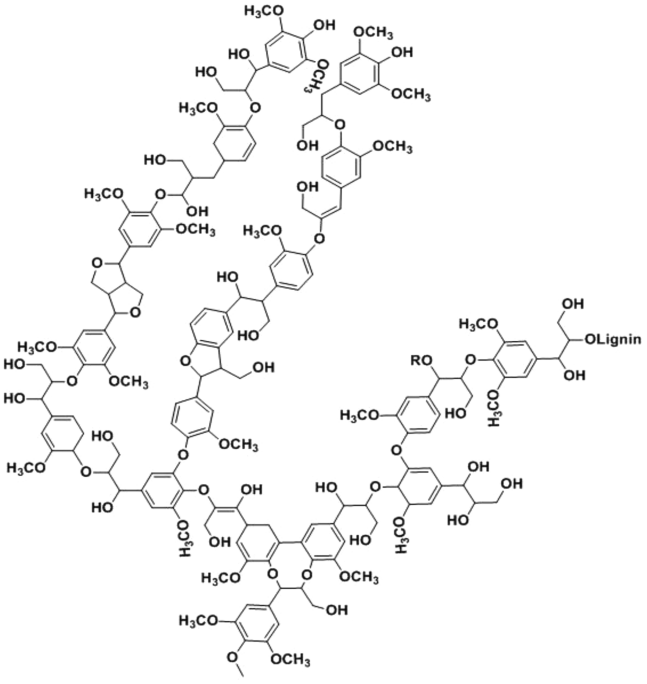

Figure 1. Molecular structure of lignin.[5]

Received: July 17, 2015
Revised: October 8, 2015
Accepted: October 9, 2015
Published: October 9, 2015

DOI: 10.1021/acs.iecr.5b02614
Ind. Eng. Chem. Res. 2015, 54, 10731−10739

certain graphitic order.[25−31] However, there has been only limited work on the utilization of lignin as a feedstock using catalysts.[32] Lignin, because of its aromatic molecular structure, presents an exciting feedstock for graphite production.[33−36]

In this paper, we present a new approach based on lignin graphitization to produce porous carbons with a graphitic framework. Our two-step conversion strategy is based on a combination of hydrothermal treatment (HTC) and catalytic graphitization steps. In the hydrothermal treatment step, lignin precursor is converted to biochar. In the catalytic graphitization step, metal nitrates are used as catalysts at low temperatures (~1000 °C). Here, the process of graphitization is thermodynamically favorable because biochar is thermodynamically less stable than graphitic carbon. When thermally unstable biochar is converted to graphitic material, the electrical conductivity of the material improves.[37,38] Carbon, without the use of any catalyst, was also prepared in the same way for comparison. The synthesized graphitic porous carbon exhibits a range of structural characteristics depending on this ability to separate each step during synthesis.[23] In addition, in this process wet lignin can be utilized, avoiding any drying costs.

2. EXPERIMENTAL SECTION

2.1. Chemicals. Lignin (Norlig A) was received from Lignotech.[39] Anhydrous ethanol (99.8%), iron(II), cobalt(II), and manganese(II) nitrate salts were purchased from Fisher Scientific. All the chemicals were used as received.

2.2. Conversion of Lignin to Graphitic Carbon. *2.2.1. Lignin Biomass to Biochar.* Biochar was prepared from lignin by hydrothermal treatment.[40] Lignin (14 g) was mixed with deionized water (100 mL) and placed in a high-temperature, high-pressure Parr reactor. The conversion was carried out at 300 °C and 1500 psi for 30 min. The temperature was selected as reported by Ramsurn et al.[40] The reactor was then allowed to cool to room temperature; here biochar, because of its hydrophobic nature, separates easily from the aqueous media. It is important to note that we have not used any catalyst during the biochar synthesis step. Yields were determined by weighing the produced biochar, which is next taken to the graphitization step. The overall conversion scheme is shown in Figure 2.

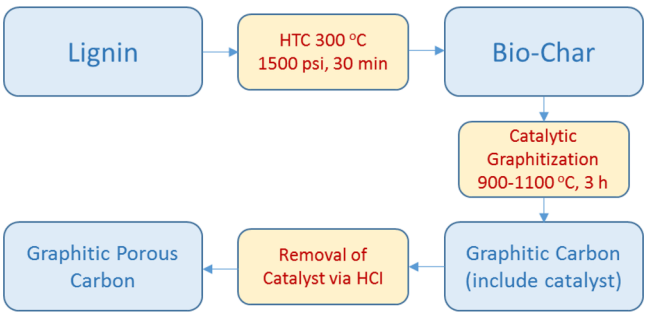

Figure 2. Conversion of lignin into graphitic carbon.

2.2.2. Catalytic Graphitization. Catalysts were added to the biochar by a solution impregnation method. Fe(II), Co(II), or Mn(II) nitrate solutions in ethanol, which were prepared in concentrations of 0.02 mol of Fe(II)NO_3 and 0.083 Mn(II)-NO_3 and Co(II)NO_3 mole-metal/g, were added to biochar. The resultant solutions were stirred at room temperature for 6 h, and then ethanol was removed under vacuum. The obtained mixtures were heated under argon at a heating rate of 20 °C/min and kept at the graphitization temperature, 900−1100 °C, for 3 h. The product was then cooled and washed with 10% (w/w) HCl to remove catalysts. The final carbon samples were labeled as MeGCx, where Me denotes the metal catalyst used and x graphitization temperature in °C. For comparison, a graphitic carbonization (GC1000) sample was processed in a similar manner but without the use of catalyst. Replication of analysis was done. Around 5% measurement error was found which comes from contamination of the high-pressure reactor (it is very hard to remove entire bio char) and the difficulty of controlling metal catalyst concentration when the solvent was removed after mixing with biochar.

2.3. Characterization. The amount of moisture (at 105 °C until the sample weight was constant), ash (combustion in nitrogen at 1000 °C), elemental analysis (carbon, oxygen (determined by difference)), and hydrogen and nitrogen components of lignin were determined by Huffman Laboratories (Golden, Colorado).The high heating value (HHV) of materials were analyzed using an IKA C 200 calorimeter. Briefly, the solid powdered sample was put in a sample holder which is a transparent capsule with a known calorific value. The sample in the capsule was located in a stainless steel crucible in a bomb calorimeter and pressurized with oxygen at 34 bar. The HHV of the sample was automatically measured by the change of temperature of water by the heat generated from total combustion of the sample. The HHV value of the sample was obtained by subtracting the total HHV value from the HHV value of the capsule. The degree of graphitization was determined by collecting X-ray diffraction (XRD) patterns on a Siemens D5000 instrument operating at 40 kV and 40 mA, using Cu Kα radiation (k = 0.15406 nm) by scanning 2θ ranging 10−70° in X-ray diffraction spectra. X-ray diffraction was used as a template analysis (for degree of graphitization) including all temperatures and catalysts; thus, the best materials were investigated for further analysis. Raman spectra were obtained with a micro-Raman spectrophotometer (Horiba, Labram HR) applying an excitation wavelength of 532 nm as the light source. X-ray photoelectron spectroscopy (XPS) analysis was performed under a ultrahigh vacuum (UHV) on a ThermoFisher ESCALAB 250 imaging X-ray photoelectron spectrometer by applying a monochromatic Al Kα (1486.68 eV) X-ray source. An internal flood gun (2 eV) and a low-energy Ar^+ external flood gun were applied for charge compensation during the data collection. The spectra were corrected using the C 1s peak at 284.6 eV. Avantage 5.932 data system used for XPS data analysis and peak fitting. Thermal stability analysis of lignin, biochar, and graphitic carbon materials was carried out on a Perkin thermogravimetric analyzer. The analyzer operated at a constant heating rate of 20 °C/min with N_2 flow (ranging from 50 to 1000 °C). Fourier transform infrared (FT-IR) spectra were collected to observe conversion of the reactants. A small amount of sample was placed directly on a Smart ATR using a Nicolet Nexus 670 FT-IR spectrometer and scanned from 4000 to 400 cm^{-1}, averaging 16 scans at 1 cm^{-1} intervals with a resolution of 4 cm^{-1}. A scanning electron microscopy instrument (SEM, Hitachi SU-70 FE-SEM) was operated at 10 kV to investigate the graphitic porous carbon structure. The Brunauer−Emmett−Teller (BET) surface area and pore size distribution of graphitic carbon materials were deduced from the isotherm analysis in a relative pressure range of 0.04−0.20 by a NOVA surface analyzer. Pore size distributions (PSD) were calculated using

DOI: 10.1021/acs.iecr.5b02614
Ind. Eng. Chem. Res. 2015, 54, 10731−10739

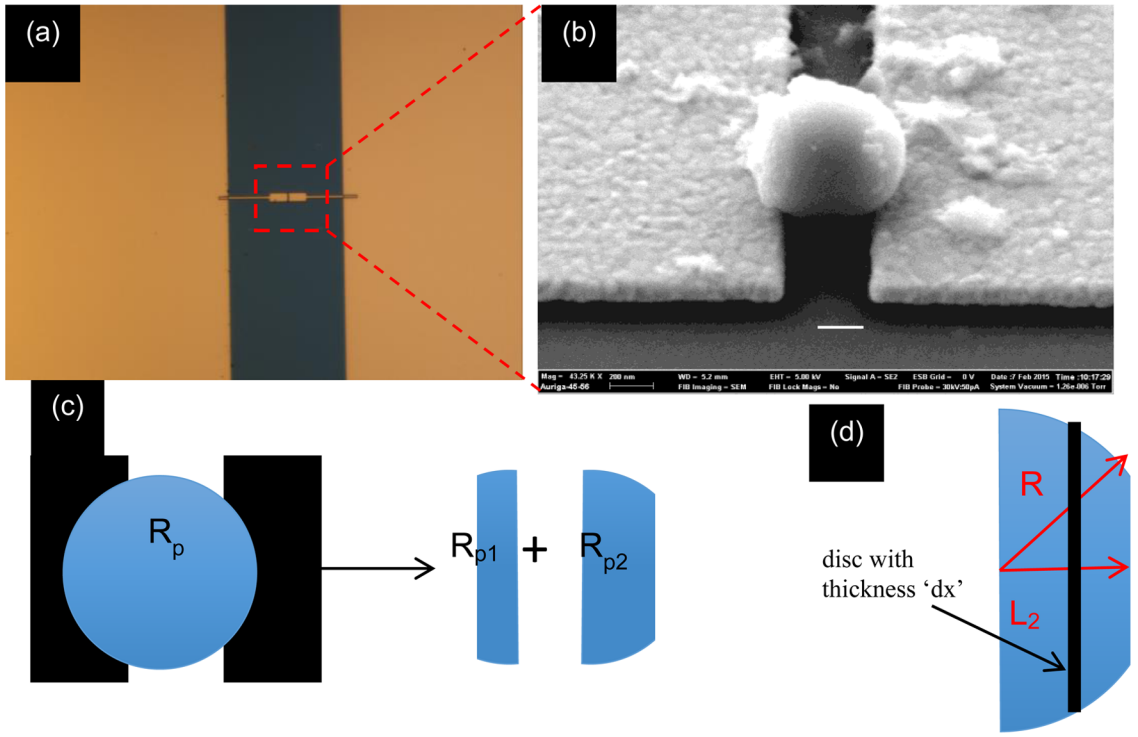

Figure 3. (a) Optical micrograph of the chip electrode design. (b) Zoomed-in region of the DEP assembly electrode region showing a single GC1000 particle bridging the electrodes. The scale bar represents 200 nm. (c) Schematic illustration of the assembled particle and its resistance as a sum of the respective suspended, interelectrode segments within the left and right hemispherical components of the particle. (d) Illustration of the geometric parameter definition used within the analytical model to extract particle conductivity values.

nonlocal density functional theory (NLDFT) on the adsorption branch.

Electrical transport properties of GC1000 and MnGC1000 particles were characterized using two-terminal current−voltage (I−V) curves. The sample preparation process involved the dielectrophoretic (DEP) assembly of individual particles across spatially separated gold nanoelectrode pairs (Figure 3), which were defined on top of thin-film nitride (100 nm) coated silicon chips using a combination of electron beam lithography and metal lift-off steps. The DEP process employed the use of nonuniform, AC electric fields to localize single graphitic particles and yield their assembly at the electric-field maxima, which is located in the interelectrode gap region near the electrode surface. The control parameters for yielding single particle localization have been published in detail elsewhere as a part of previous studies involving one-dimensional constructs derived from manganese oxide and carbon material systems.[41−43] Briefly, an AC bias is applied across the nanoelectrode pair and a droplet, which contains a colloidal suspension of the graphitic particles in ethanol, is placed on the chip. As a result of the applied electric field, the particles become polarized and the induced dipole experiences a dielectrophoretic force. This DEP force attracts the particles toward the electric field maxima and yields their assembly on top of the gold nanoelectrodes. After assembly, the chip is dried using a nitrogen gun. The GC1000 particles were assembled by applying a 4 V bias at 1 kHz for 2 min. On the other hand, MnGC1000 particles were assembled using a 3 V bias at 1 kHz for 2 min. Representative images of the chip design and an assembled GC1000 particle are shown in Figure 3a,b.

3. RESULTS AND DISCUSSION

3.1. Molecular and Thermal Properties. Elemental, calorimetric (HHV) analysis results of lignin, biochar, and graphitic carbon materials are listed in Tables 1 and 2. The HHV content increased during the hydrothermal treatment and catalytic graphitization step. Similar trends occur with

Table 1. Elemental Analysis of Lignin

Element	Amount (wt%)	
C	42.80	Dry Basis
H	4.80	
S	6.6	
N	0.13	
O	39.66	
Moisture	9.21	
Ash	10.20	

Table 2. Heating Value of the Carbon[a]

carbon sample	HHV (kJ/g)
lignin biomass	18
GC1000	26
MnGC900	26
MnGC1000	29

[a]HHV, high heating value.

DOI: 10.1021/acs.iecr.5b02614
Ind. Eng. Chem. Res. 2015, 54, 10731−10739

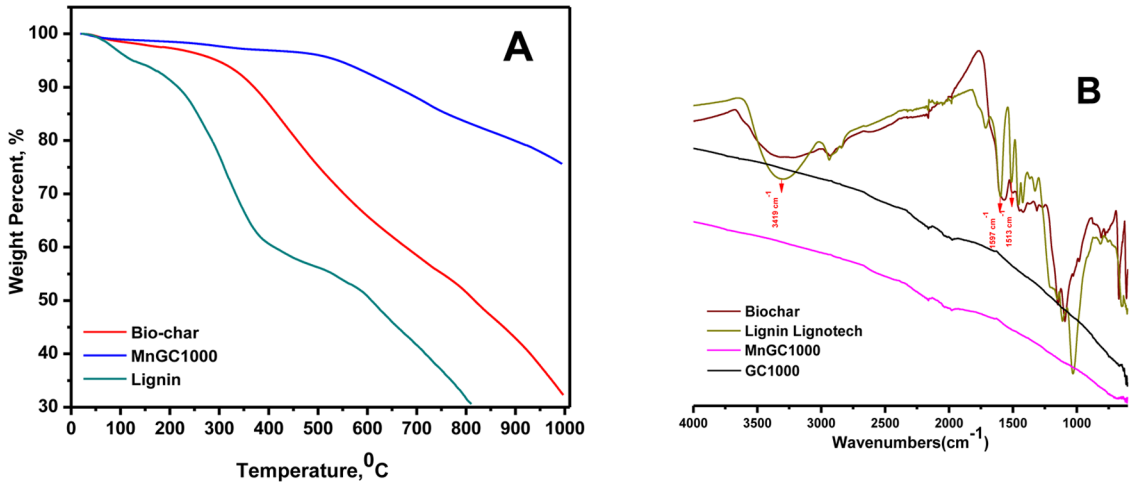

Figure 4. (A) Thermogravimetric analyses of MnGC1000, biochar, and lignin. (B) FT-IR spectra (transmission versus wavenumber) of lignin, biochar, GC1000, and MnGC1000.

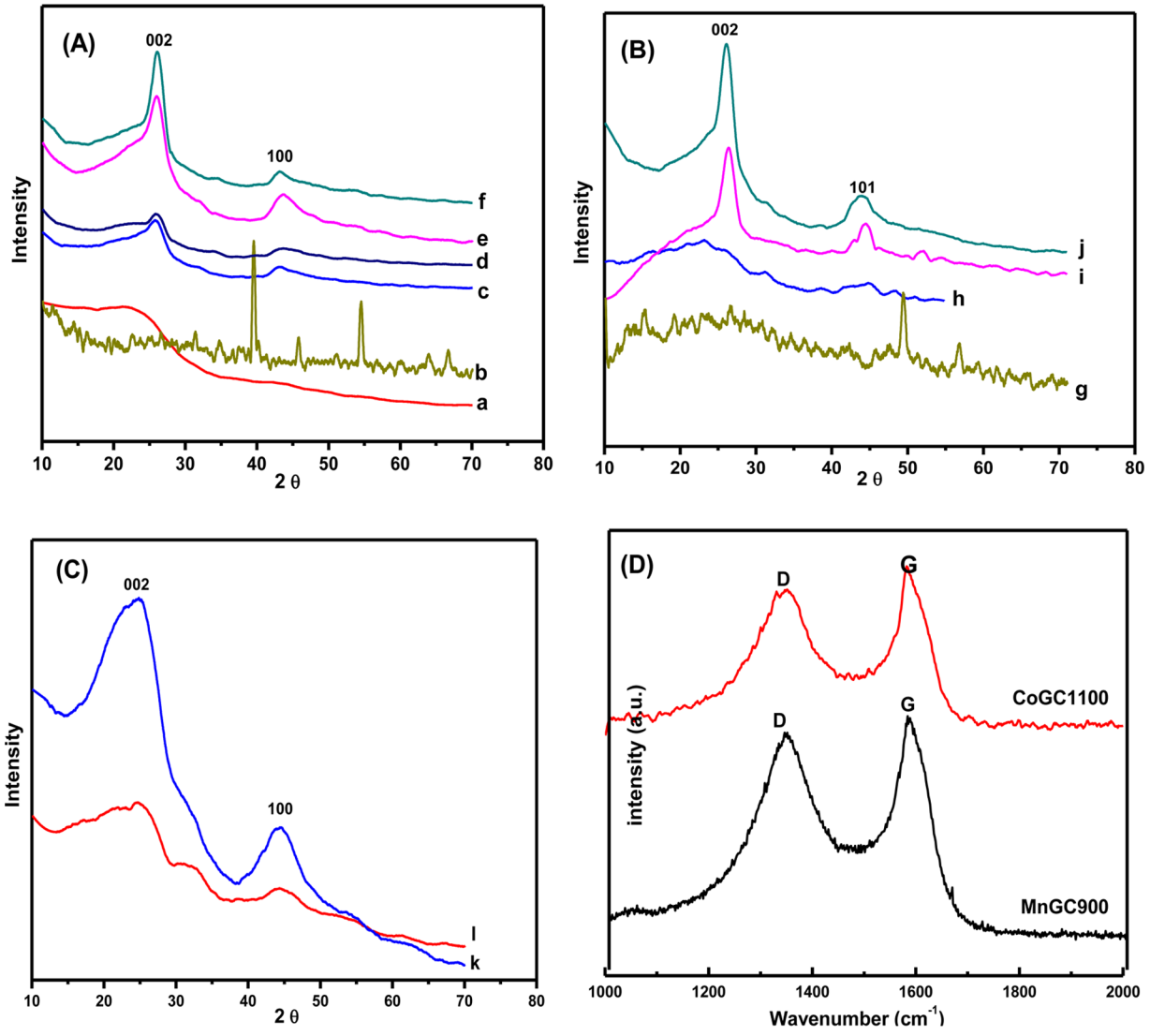

Figure 5. (A–C) XRD patterns of the carbon samples: (a) biochar, (b) MnGC1000 (before metal removal), (c) GC1000, (d) MnGC1100, (e) MnGC1000, (f) MnGC900, (g) CoGC1000 (before metal removal), (h) CoGC900, (i) CoGC1000, (j) CoGC1100, (k) FeGC1100, and (l) FeGC1000. (D) Raman spectrum of the MnGC9000 and CoGC1100.

DOI: 10.1021/acs.iecr.5b02614
Ind. Eng. Chem. Res. 2015, 54, 10731–10739

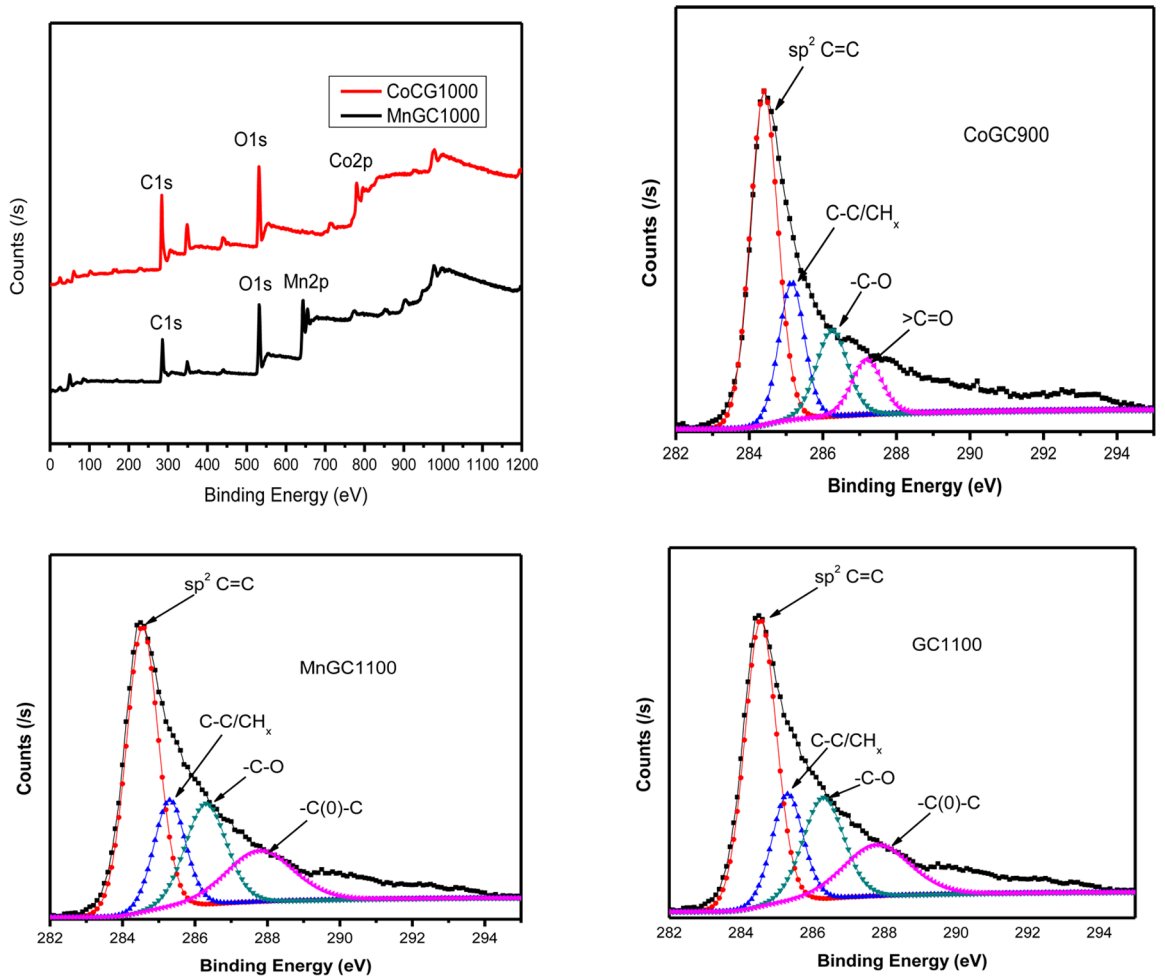

Figure 6. XPS spectra of the CoGC1100, MnGC900, and GC1100.

graphitization (noncatalyst) at 1000 °C with a value of 26 kJ/g. MnGC1000 shows the highest HHV values of 29 kJ/g, which is due to the removal of more oxygen during the catalytic graphitization steps. The average weight losses during the HTC step was about 64 wt %, and that during the graphitization step was 50 wt %.

Results of the thermogravimetric analysis are shown in Figure 4A. The initial mass loss in lignin corresponds to the loss of adsorbed water during heating. Similar trends were observed for biochar and MnGC1000. MnGC1000 has a high thermal stability due to its higher graphitic carbon content. Thus, carbons produced using metal nitrate catalysts have high thermal stability.

Lignin, biochar, GC1000, and Mn1000 samples were characterized by infrared spectroscopy in the near IR region (4000−600 cm^{-1}) as shown in Figure 4B. Various bands in the spectrum were identified as corresponding to OH (3418 cm^{-1}), methoxyl (2843 cm^{-1}), aliphatic CH (3000−2861 cm^{-1}), and aromatic CH (3064 cm^{-1}) groups as well as aromatic rings (1512 and 1597 cm^{-1}). The most characteristic bands of lignin were at 1513 and 1597 cm^{-1} (aromatic ring vibrations) and between 1470 and 1460 cm^{-1} (CH deformation). The intensity of the −OH band decreased with hydrothermal treatment and disappeared completely with the graphitization process because of the loss of phenolic and alcoholic groups. Similar trends for the OH, OCH_3, aliphatic CH, and aromatic rings ratios are observed. In short, all the functional groups of the lignin disappeared after catalytic graphitization.

3.2. Crystallographic Properties. The XRD patterns in the wide-angle region (10°−70°) permit an evaluation of the graphitic nature of the synthesized carbons. The XRD patterns of the graphitic carbons are shown in Figure 5. As a reference, the XRD pattern of biochar (a) and noncatalysis GC1000 sample (c) are also shown. As expected, biochar (a) reveals almost no diffraction peak and GC1000 (c) exhibited only small characteristics of graphited carbon diffraction peak. These results are consistent with an amorphous framework. In contrast, the metal catalyzed carbons show intense XRD peaks at around $2\theta = 26°$ and 44°. These peaks can be assigned to the (002) and (101) diffractions of a graphitic framework.[44] These results indicate that the formation of graphitic structures is promoted by heat treatment in the presence of metal nitrate catalysts. Similar results have been reported previously for graphitic carbons generated from metal-impregnated polymeric gels, aerogels, and biosource materials.[23−26] As shown in Figure 5 (left), MnGCs exhibited the largest graphitic carbon peaks among the three types of metal nitrate catalysts. In the case of MnGCs, MnGC900 (f) showed a sharper peak than MnGC1000 (e) and MnGC1100 (d). Although the MnGC900 has lower HHV value than MnGC1000 shown in Table 2, it is found that the degree of biochar graphitization by manganese(II) nitrate impregnation is greater at the lower temperature because more amorphous carbon remains in the

DOI: 10.1021/acs.iecr.5b02614
Ind. Eng. Chem. Res. 2015, 54, 10731−10739

MnGC1000 structure. This is attributed to the high number of oxygenated functional groups in the carbons at low carbonization temperatures.[23] This presumably favors the reduction of metallic salts and formation of metal particles at relatively low temperatures.

For the case of cobalt nitrate catalysis, the graphitization process started at 900 °C (h) and almost stopped at 1000 °C (i). As a result, increasing the temperature did not increase the graphitization. Graphitic carbon formation via iron nitrate catalysis requires a higher temperature of around 1100 °C (k) and shows a higher XRD peak than graphitic carbon at 1000 °C (l). The samples before acid wash still contain the metal originating from the catalyst. Mn and MnO (b) particles appear at around 39°, 45°, and 54°; and Co and CoO (g) particles appear at 49° and 58°, in XRD.[45]

The graphitic carbon structures are formed by a series of steps in the catalytic process. When the biochar with metal salt is heated, the salt decomposes to form the corresponding metallic oxides such as MnO and CoO. With continued heating, the carbon−oxygen−metal structure reduces to a metal−carbon structure. When the temperature reaches 900 °C or higher, the transformation of carbon from amorphous into a more ordered graphitic structure occurs, both catalyzed by metal and metal oxide particles.[23] Moreover, according to ref 46, group IVb−VIIb metals on the periodic table are called graphitization catalyst metals because they have 2−5 electrons in the d-shell orbital, which make them capable of forming strong bonds between metal carbides and carbon-based materials. On the other hand, group VIII metals have 6−10 electron in their d-shell orbital, which makes them less active in terms of accepting electrons from carbon-based materials. This is consistent with our results that manganese (in VIIb group) shows a degree of graphitization higher than that of cobalt- and iron-based catalysts (in VIII group).

The nature of graphitization of carbon materials were further evaluated by Raman spectroscopy. The application of Raman as an evaluation degree of graphite was first reported by Tuinstra and Koenig.[47] The D band at around 1350 cm^{-1} corresponds to disordered graphitic lattice (A_{1g} symmetry).The D band which is in Raman inactive mode is related to loss of hexagonal symmetry in the graphite structure. The G band at around 1578 cm^{-1} is associated with the vibration of the ideal graphite lattice (E_{2g} symmetry)[48] shown on Figure 5 D. The G band which is in Raman active mode is referred to 2-dimensional high crystalline network structure. The intensity ratio of G band to D band (I_g/I_d) is a good indicator of degree of graphitization for carbon-based materials. The I_g/I_d values were 1.1 and 1 for MnGC1000 and CoGC1000, respectively, which are higher than or comparable to previously reported data.[25,28,29,38,44,49,50]

The elemental analysis and the nature of carbon materials were detected by XPS spectroscopy shown in Figure 6 and Table 3. The carbon content of materials were 64, 64.9, and 50.4 for GC1100, CoGC1100 and MnGC900, respectively. The carbon types of materials classified such as graphitized carbon, that is, the C═C groups (E_B = 284.4 eV) and other forms of carbon (amorphous carbons) which are, i.e., C−C/CH_x groups (E_B = 285.1 eV), −C−O (E_B = 286.2 eV) and >C═O (E_B = 287.2 eV).[30,51] Although the GC1100 has higher carbon content on the surface than the metal catalyzed graphitic carbon, the MnGC900 and CoGC1100 show higher ratio of the graphitized carbon to amorphous carbon than the GC1100. The ratios of the graphitized carbon to amorphous carbon were 0.45, 0.53, and 0.60 for GC1100, CoGC1100, and MnGC900, respectively, which demonstrate that the formation of graphitic carbon was enhanced by including metal nitrate catalyst in the graphitization step.

Table 3. XPS Analysis Result of the CoGC1100, MnGC900, and GC1100

materials	C	O	metal catalyst	C═C	C−C	−C−O
GC1100	64.0	27.7	–	45.3	16.8	20.8
CoGC1100	64.9	32.3	2.1	53.7	20.8	13.7
MnGC900	50.4	39.8	9.6	60.7	21.9	9.4

3.3. Morphology and Pore Structure. The SEM micrographs of biochar, GC1000, MnGC900 (with metal), and MnGC900 (without metal) are shown in Figure 7. Biochar

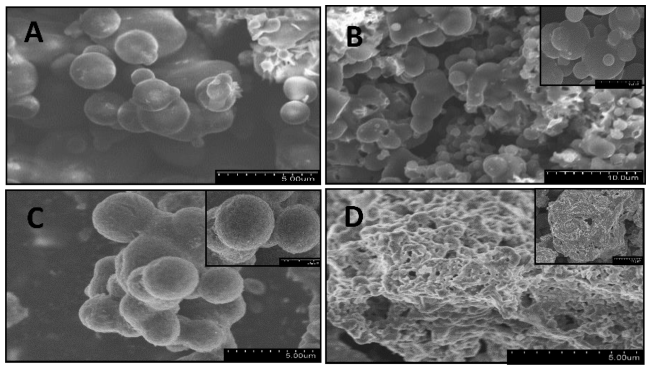

Figure 7. Scanning electron micrographs of (a) biochar, (b) GC1000, (c) MnGC1000, and (d) MnGC1000 (before metal removal).

particles are spherical in shape and are 4 μm in diameter. GC1000 are globular precipitated solids with 1−3 μm diameters, and MnGC900 solids are also globular with 2 μm diameters. Figure 7d shows SEM images of MnGC900 before acid washing, where a metal−carbon mixed structure is prominent. From the SEM micrographs of materials, the distribution of particle sizes within an order of magnitude is consistent with results observed for hydrothermal synthesis of particles. Also, we do not expect any size dependence on the properties of these materials because this is expected to occur only when their size extends within the nanometer-regime. At these size scales, we believe that the properties are largely determined by the degree of graphitization.

To probe porosity, nitrogen sorption−desorption isotherms were collected for CoGC1000, FeGC900, GC1000, and MnGC1000 graphitic carbons, as depicted in Figure 8. The Brunauer−Emmett−Teller surface area (SA_{BET}) of graphitic carbons was found to be in the range of 150−250 $m^2\ g^{-1}$ as summarized in Table 4. The surface area and pore size distributions of the GC1000 are similar to those of MnGC1000. FeGC1000 showed higher surface area than GC1000, most likely because Fe-based catalysis is more effective on surface activation. The pore size distribution curves (Figure 8, inset) show that MeGCs and GC1000 have major PSD peaks in the microporous and mesoporous ranges, suggesting that the resulting carbons have meso- and microporous structures.

3.4. Electrical Properties. A Keithley 2636B source meter was employed to probe the $I-V$ behavior of individual particles. For instance, the $I-V$ curves extracted from representative, single GC1000 and MnGC1000 particles are shown in Figure 9. From the linear behavior of these plots, it is evident that an

DOI: 10.1021/acs.iecr.5b02614
Ind. Eng. Chem. Res. 2015, 54, 10731−10739

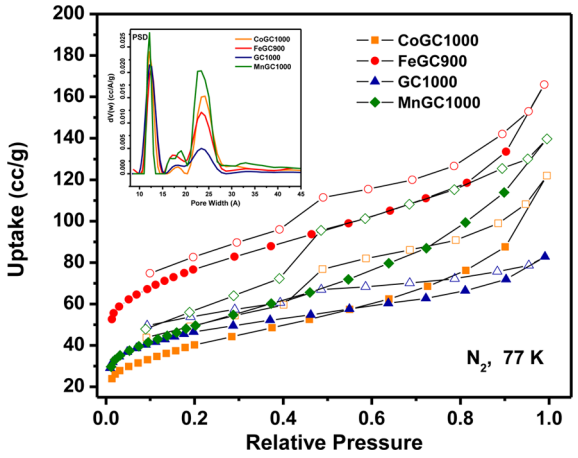

Figure 8. Nitrogen sorption isotherm and pore size distribution (inset) of graphitic porous carbons.

Table 4. Properties of the Produced Graphitic Carbon Materials

material	XRD (deg. of crystallinity)	I_G/I_D	pore size (nm)	surface area ($m^2 g^{-1}$)	comment
GC1000	low		1.2, 2.3	164	low electrical conductivity
MnGC900	high				high electrical conductivity
MnGC1000	high	1.1	1.2, 2.3	169	
MnGC1100	medium				
CoGC900	medium				
CoGC1000	high	1.1	1.2, 2.3	136	
CoGC1100	high				
FeGC1000	medium		1.2, 2.3	272	high surface area
FeGC1100	medium				

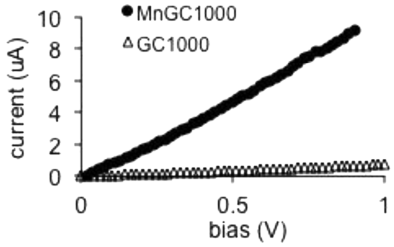

Figure 9. $I-V$ data acquired from individual MnGC1000 and GC1000 particles.

ohmic contact is established between the metal electrode and the graphitic particle. Furthermore, the MnGC1000 particle exhibits a much larger current (an order of magnitude higher) as compared to the GC1000 particle. This substantive increase in electric currents implies a higher electronic conductivity for the MnGC1000 particle, as compared to the GC1000 particle, and is attributed to its higher graphitic content as observed previously within the XRD data (Figure 6). To extract the electronic conductivity of the particle from its resistance value, we have employed an analytical model for the resistance (R_p) of the particle segment, which spans the interelectrode gap and contributes to electric transport within this device. This is schematically shown in Figure 3c,d, where the assembled particle has a radius R and an interelectrode suspended length of L_1 and L_2 within the left and right hemispherical components of the particle, respectively. The overall resistance of the particle is the sum of the individual contributions, which arise from the suspended segments of its left-side and right-side hemispherical components. The resistance of each hemispherical component of the particle is obtained by integrating the contributions from infinitesimally thin circular discs that span its thickness (Figure 3d). For instance, the resistance of the suspended segment of the left-side hemispherical particle is calculated as

$$R_{p1} = \int_{L_1}^{0} \frac{\rho\, dx}{A} = \frac{\rho}{\pi} \int_{L_1}^{0} \frac{dx}{R^2 - x^2} = \frac{\rho}{2\pi R} \ln\left(\frac{R + L_1}{R - L_1}\right) \quad (1)$$

Thus, the overall resistance of the interelectrode suspended segment of the particle is given as

$$R_p = R_{p1} + R_{p2} = \frac{\rho}{2\pi R}\left\{\ln\left(\frac{R + L_1}{R - L_1}\right) + \ln\left(\frac{R + L_2}{R - L_2}\right)\right\} \quad (2)$$

While the particle resistance is obtained from the $I-V$ curves of Figure 9, the geometric parameters such as R, L_1, and L_2 are extracted from the SEM image of the assembled particle (Figure 3). When these values are substituted in eq 2, the values for particle resistivity and conductivity can be obtained for representative GC1000 and MnGC1000 particles. These values, which are listed in Table 5, point to an order of magnitude higher value for the conductivity of a MnGC1000 particle as compared to GC1000 particle because of its higher graphitic content. It is important to note that this electrical conductivity measurement approach involving single particles represents an improvement over past reports, which have employed bulk-scale aggregates or powders of particles. This is because measurements with aggregates of particles not only are influenced by the intrinsic conductivity of the particle, but also are impacted by the interparticle transport impedances. On the other hand, our approach with single particles provides insights into the conductivity of the particle while isolating the interparticle transport impedance.

4. CONCLUSIONS

Lignin can be successfully converted to graphitic carbon via hydrothermal carbonization followed by catalytic graphitization. Cobalt and manganese are better graphitization catalysts than iron. In addition, the extent of graphitization is dependent on the temperature. A good quality graphitic carbon was obtained using catalysis by $Mn(NO_3)_2$ at 900 °C and $Co(NO_3)_2$ at 1100 °C. The produced material is free of lignin-functional groups,

Table 5. Electronic Conductivity Results of MnGC1000 and GC1000 Particles

particle type	radius (R, nm)	L_1 (nm)	L_2 (nm)	resistance (R_p, kohm)	resistivity (ohm·m)	conductivity ($S \cdot m^{-1}$)
MnGC1000	430	362	81	98.8	0.094	10.6
GC1000	346	222	187	1306.8	1.04	0.96

DOI: 10.1021/acs.iecr.5b02614
Ind. Eng. Chem. Res. 2015, 54, 10731−10739

shows high electrical conductivity, has both micro- and mesoporous structures, and is thermally stable.

AUTHOR INFORMATION

Corresponding Author

*E-mail: rbgupta@vcu.edu. Phone: (804)-828-1211.

Present Address

#(M.D.) Department of Chemical Engineering, Osmaniye Korkut Ata University, 80000 Osmaniye, Turkey.

Notes

The authors declare no competing financial interest.

ACKNOWLEDGMENTS

M.D. thanks the Ministry of National Educational of Republic of Turkey for his graduate fellowship. Experimental assistance from Dr. Gokul Vasudevamurty is appreciated. This work was partly supported by the National Science Foundation under Grant 1266438. This work was performed, in part, at the Sandia-Los Alamos Center for Integrated Nanotechnologies (CINT), a U.S. Department of Energy, and Office of Basic Energy Sciences user facility. The chip nanofabrication activities were performed at CINT under the user proposal U2014A0084. Sandia National Laboratories is a multiprogram laboratory operated by Sandia Corporation, a wholly owned subsidiary of Lockheed Martin Company, for the U.S. Department of Energy's National Nuclear Security Administration under contract DE-AC04-94AL85000. H.M.E acknowledges research support by the U.S. Department of Energy, Office of Basic Energy Sciences under award number (DE-SC0002576).

REFERENCES

(1) Gosselink, R. J. A.; et al. Analytical protocols for characterisation of sulphur-free lignin. *Ind. Crops Prod.* **2004**, *19* (3), 271−281.

(2) Boeriu, C. G.; et al. Characterisation of structure-dependent functional properties of lignin with infrared spectroscopy. *Ind. Crops Prod.* **2004**, *20* (2), 205−218.

(3) Lora, J.; Glasser, W. Recent Industrial Applications of Lignin: A Sustainable Alternative to Nonrenewable Materials. *J. Polym. Environ.* **2002**, *10* (1−2), 39−48.

(4) Duku, M. H.; Gu, S.; Hagan, E. B. A comprehensive review of biomass resources and biofuels potential in Ghana. *Renewable Sustainable Energy Rev.* **2011**, *15* (1), 404−415.

(5) Chakar, F. S.; Ragauskas, A. J. Review of current and future softwood kraft lignin process chemistry. *Ind. Crops Prod.* **2004**, *20* (2), 131−141.

(6) Hon, D. N. S. *Chemical Modification of Lignocellulosic Materials*; Marcel Dekker, Inc.: New York, 1996.

(7) Smolarski, N. *High-value opportunities for lignin: Unlocking its potential*; Frost & Sullivan: Paris, 2012.

(8) Laurichesse, S.; Avérous, L. Chemical modification of lignins: Towards biobased polymers. *Prog. Polym. Sci.* **2014**, *39* (7), 1266−1290.

(9) Stewart, D. Lignin as a base material for materials applications: Chemistry, application and economics. *Ind. Crops Prod.* **2008**, *27* (2), 202−207.

(10) Mansouri, N.-E. E.; Salvadó, J. Structural characterization of technical lignins for the production of adhesives: Application to lignosulfonate, kraft, soda-anthraquinone, organosolv and ethanol process lignins. *Ind. Crops Prod.* **2006**, *24* (1), 8−16.

(11) Wu, Y.; et al. Adsorption of chromium(III) on lignin. *Bioresour. Technol.* **2008**, *99* (16), 7709−7715.

(12) Toledano, A.; et al. Heterogeneously Catalysed Mild Hydrogenolytic Depolymerisation of Lignin Under Microwave Irradiation with Hydrogen-Donating Solvents. *ChemCatChem* **2013**, *5* (4), 977−985.

(13) The International Lignin Institute. http://www.ili-lignin.com/. 2010.

(14) Kadam, K. L.; Chin, C. Y.; Brown, L. W. Continuous biomass fractionation process for producing ethanol and low-molecular-weight lignin. *Environ. Prog. Sustainable Energy* **2009**, *28* (1), 89−99.

(15) Suhas; Carrott, P. J. M.; Ribeiro Carrott, M. M. L. Lignin − from natural adsorbent to activated carbon: A review. *Bioresour. Technol.* **2007**, *98* (12), 2301−2312.

(16) Zaldivar, R. J.; Rellick, G. S. Some observations on stress graphitization in carbon-carbon composites. *Carbon* **1991**, *29* (8), 1155−1163.

(17) Fu, T.; Lv, J.; Li, Z. Effect of Carbon Porosity and Cobalt Particle Size on the Catalytic Performance of Carbon Supported Cobalt Fischer−Tropsch Catalysts. *Ind. Eng. Chem. Res.* **2014**, *53* (4), 1342−1350.

(18) Ōya, A.; Ōtani, S. Catalytic graphitization of carbons by various metals. *Carbon* **1979**, *17* (2), 131−137.

(19) Marsh, H.; Crawford, D.; Taylor, D. W. Catalytic graphitization by iron of isotropic carbon from polyfurfuryl alcohol, 725−1090 K. A high resolution electron microscope study. *Carbon* **1983**, *21* (1), 81−87.

(20) Logeswari, J.; Pandurangan, A.; Sangeetha, D. An Efficient Catalyst for the Large Scale Production of Multi-Walled Carbon Nanotubes. *Ind. Eng. Chem. Res.* **2011**, *50* (23), 13347−13354.

(21) Lei, Z.; et al. Nickel-Catalyzed Fabrication of SiO2, TiO2/Graphitized Carbon, and the Resultant Graphitized Carbon with Periodically Macroporous Structure. *Chem. Mater.* **2007**, *19* (3), 477−484.

(22) Maldonado-Hódar, F. J.; et al. Catalytic Graphitization of Carbon Aerogels by Transition Metals. *Langmuir* **2000**, *16* (9), 4367−4373.

(23) Sevilla, M.; Fuertes, A. B. Catalytic graphitization of templated mesoporous carbons. *Carbon* **2006**, *44* (3), 468−474.

(24) Huang, C.-h.; et al. Dual-template synthesis of magnetically-separable hierarchically-ordered porous carbons by catalytic graphitization. *Carbon* **2011**, *49* (9), 3055−3064.

(25) Liu, Y.; et al. Highly porous graphitic materials prepared by catalytic graphitization. *Carbon* **2013**, *64* (0), 132−140.

(26) Zhai, D.; et al. Porous graphitic carbons prepared by combining chemical activation with catalytic graphitization. *Carbon* **2011**, *49* (2), 725−729.

(27) Shi, K.; et al. Catalyst-Free Synthesis of Multiwalled Carbon Nanotubes via Microwave-Induced Processing of Biomass. *Ind. Eng. Chem. Res.* **2014**, *53* (39), 15012−15019.

(28) Gutiérrez-Pardo, A.; et al. Characterization of porous graphitic monoliths from pyrolyzed wood. *J. Mater. Sci.* **2014**, *49* (22), 7688−7696.

(29) Sevilla, M.; et al. Direct synthesis of graphitic carbon nanostructures from saccharides and their use as electrocatalytic supports. *Carbon* **2008**, *46* (6), 931−939.

(30) Sevilla, M.; Fuertes, A. B. Graphitic carbon nanostructures from cellulose. *Chem. Phys. Lett.* **2010**, *490* (1−3), 63−68.

(31) Li, R.; et al. Formation of Nitrogen-Doped Mesoporous Graphitic Carbon with the Help of Melamine. *ACS Appl. Mater. Interfaces* **2014**, *6* (23), 20574−20578.

(32) Kubo, S.; Uraki, Y.; Sano, Y. Catalytic graphitization of hardwood acetic acid lignin with nickel acetate. *J. Wood Sci.* **2003**, *49* (2), 188−192.

(33) Chatterjee, S.; et al. Conversion of Lignin Precursors to Carbon Fibers with Nanoscale Graphitic Domains. *ACS Sustainable Chem. Eng.* **2014**, *2* (8), 2002−2010.

(34) Chatterjee, S.; et al. Synthesis and characterization of lignin-based carbon materials with tunable microstructure. *RSC Adv.* **2014**, *4* (9), 4743−4753.

(35) Popova, O. V.; Serbinovskii, M. Y. Graphite from hydrolysis lignin: Preparation procedure, structure, properties, and application. *Russ. J. Appl. Chem.* **2014**, *87* (6), 818−823.

DOI: 10.1021/acs.iecr.5b02614
Ind. Eng. Chem. Res. 2015, 54, 10731−10739

(36) Vivekanandhan, S.; Misra, M.; Mohanty, A. K. Microscopic, structural, and electrical characterization of the carbonaceous materials synthesized from various lignin feedstocks. *J. Appl. Polym. Sci.* **2015**, *132*, 1−9.
(37) Fischbach, D.; Walker, P., Jr. *Chemistry and physics of carbon*; Marcel Dekker: New York, 1971; Vol. *7*, p 1.
(38) Tang, J.; et al. Effect of transition metal on catalytic graphitization of ordered mesoporous carbon and Pt/metal oxide synergistic electrocatalytic performance. *Microporous Mesoporous Mater.* **2013**, *177* (0), 105−112.
(39) LignoTech Home Page. http://www.lignotech.com/ (accessed 2015).
(40) Ramsurn, H.; Kumar, S.; Gupta, R. B. Enhancement of biochar gasification in alkali hydrothermal medium by passivation of inorganic components using Ca (OH) 2. *Energy Fuels* **2011**, *25* (5), 2389−2398.
(41) Subramanian, A.; et al. On-chip lithium cells for electrical and structural characterization of single nanowire electrodes. *Nanotechnology* **2014**, *25* (26), 265402.
(42) Didi, X.; et al. Shaping Nanoelectrodes for High-Precision Dielectrophoretic Assembly of Carbon Nanotubes. *IEEE Trans. Nanotechnol.* **2009**, *8* (4), 449−456.
(43) Palapati, N. K. R.; Pomerantseva, E.; Subramanian, A. Single nanowire manipulation within dielectrophoretic force fields in the sub-crossover frequency regime. *Nanoscale* **2015**, *7* (7), 3109−3116.
(44) Wang, Z. L.; et al. Co-gelation synthesis of porous graphitic carbons with high surface area and their applications. *Carbon* **2011**, *49* (1), 161−169.
(45) Fu, R.; et al. Formation of Graphitic Structures in Cobalt- and Nickel-Doped Carbon Aerogels. *Langmuir* **2005**, *21* (7), 2647−2651.
(46) Ōya, A.; Marsh, H. Phenomena of catalytic graphitization. *J. Mater. Sci.* **1982**, *17* (2), 309−322.
(47) Tuinstra, F.; Koenig, J. L. Raman Spectrum of Graphite. *J. Chem. Phys.* **1970**, *53* (3), 1126−1130.
(48) Sadezky, A.; et al. Raman microspectroscopy of soot and related carbonaceous materials: spectral analysis and structural information. *Carbon* **2005**, *43* (8), 1731−1742.
(49) Xiong, H.; et al. Graphitic-Carbon Layers on Oxides: Toward Stable Heterogeneous Catalysts for Biomass Conversion Reactions. *Angew. Chem., Int. Ed.* **2015**, *54* (27), 7939−7943.
(50) Qin, H.; et al. Lignin based synthesis of carbon nanocages assembled from graphitic layers with hierarchical pore structure. *Mater. Lett.* **2015**, *159*, 463−465.
(51) Okpalugo, T. I. T.; et al. High resolution XPS characterization of chemical functionalised MWCNTs and SWCNTs. *Carbon* **2005**, *43* (1), 153−161.

DOI: 10.1021/acs.iecr.5b02614
Ind. Eng. Chem. Res. 2015, 54, 10731−10739